The metal-poor dwarf irregular galaxy candidate next to Mrk 1172

Augusto E. Lassen [ID],[1]★ Rogerio Riffel [ID],[1] Ana L. Chies-Santos [ID],[1] Evelyn Johnston,[2,3] Boris Häußler,[4] Gabriel M. Azevedo,[1] Daniel Ruschel-Dutra [ID][5] and Rogemar A. Riffel [ID][6]

[1]*Universidade Federal do Rio Grande do Sul, Departamento de Astronomia, Av. Bento Gonçalves 9500, Porto Alegre, RS, Brazil*
[2]*Universidad Diego Portales, Núcleo de Astronomía de la Facultad de Ingeniería y Ciencias, Av. Ejército Libertador 441, Santiago, Chile*
[3]*Pontificia Universidad Católica de Chile, Institute of Astrophysics, Av. Vicuña Mackenna 4860, 7820436 Macul, Santiago, Chile*
[4]*European Southern Observatory, Alonso de Córdova 3107, Vitacura, Santiago, Chile*
[5]*Universidade Federal de Santa Catarina, Departamento de Física, P.O. Box 476, 88040-900, Florianópolis, SC, Brazil*
[6]*Universidade Federal de Santa Maria, Departamento de Física, Centro de Ciências Naturais e Exatas, 97106-900 Santa Maria, RS, Brazil*

ABSTRACT

In this work, we characterize the properties of the object SDSS J020536.84−081424.7, an extended nebular region with projected extension of 14×14 kpc^2 in the line of sight of the ETG Mrk 1172, using unprecedented spectroscopic data from MUSE. We perform a spatially resolved stellar population synthesis and estimate the stellar mass for both Mrk 1172 (1×10^{11} M$_\odot$) and our object of study (3×10^9 M$_\odot$). While the stellar content of Mrk 1172 is dominated by an old ($\sim$10 Gyr) stellar population, the extended nebular emission has its light dominated by young to intermediate age populations (from $\sim$100 Myr to $\sim$1 Gyr) and presents strong emission lines such as H β; [O III] $\lambda\lambda$4959, 5007 Å; H α; [N II] $\lambda\lambda$6549, 6585 Å; and [S II] $\lambda\lambda$6717, 6732 Å. Using these emission lines, we find that it is metal poor (with $Z \sim 1/3\,Z_\odot$, comparable to the LMC) and is actively forming stars (0.70 M$_\odot$ yr^{-1}), especially in a few bright clumpy knots that are readily visible in H α. The object has an ionized gas mass $\geq 3.8 \times 10^5$ M$_\odot$. Moreover, the motion of the gas is well described by a gas in circular orbit in the plane of a disc and is being affected by interaction wtih Mrk 1172. We conclude that SDSS J020536.84−081424.7 is most likely a dwarf irregular galaxy (the dIGal).

Key words: ISM: abundances – H II regions – galaxies: dwarf.

1 INTRODUCTION

Dwarf galaxies are the most abundant class of galaxies in the Universe, and play a fundamental role in models of galaxy formation and evolution. In the hierarchical framework of galaxy formation, they are the building blocks of larger objects, contributing to the assembly of larger galaxies via successive mergers (e.g. Mateo 1998; Revaz & Jablonka 2018; Digby et al. 2019; and references therein). Since these galaxies are numerous, they probe many different environmental conditions and are sensitive to perturbations such as stellar feedback, for example, because their shallower gravitational potential wells make the pressure of the gas within these galaxies lower when compared to more massive galaxies (Navarro, Eke & Frenk 1996; Mashchenko, Wadsley & Couchman 2008). While some dwarf galaxies may evolve in isolation, many of them are found within systems where the effects of tidal and ram-pressure forces, for example, leave imprints in their star formation histories (SFHs). In the former case, these objects represent ideal laboratories to study internal drivers of galaxy evolution, like gas accretion (van Zee 2001; van Zee & Haynes 2006; Bernard et al. 2010; González-Samaniego et al. 2014). In the latter case, these compose an important set of galaxies to study the effects of environment in the determination of the mass and the structure of satellites (Mayer et al. 2001; Kazantzidis et al. 2011; Fattahi et al. 2018; Steyrleithner, Hensler & Boselli 2020).

Traditionally, dwarf galaxies are classified in two main categories, the dwarf Irregular (dI) and the dwarf Spheroidal (dSph). The dI galaxies are rich in gas and actively forming stars, usually located in the field, while dSph galaxies do not present significant star formation activity (Mayer et al. 2001; Gallart et al. 2015). The differences between both categories of dwarfs are usually based on current properties, and probably do not reflect their evolutionary histories. Since dIs and dSphs share many structural and evolutionary properties, the categorization is most likely to be related to the fact that in dSphs the star formation (SF) has ceased recently, while in dIs this SF persists until the present day (Skillman & Bender 1995; Kormendy & Bender 2012; Kirby et al. 2013).

In general, dIs are metal-poor, and the abundance of heavy elements in these galaxies, measured from their H II regions, lies in the range of 1/3–1/40 Z$_\odot$ (Kunth & Östlin 2000). As examples of metal-poor dIs we have the SMC and the LMC, with a metallicity of roughly 1/8 Z$_\odot$ and 1/3 Z$_\odot$, respectively (Kunth & Östlin 2000). There are also the blue compact dwarf galaxies (BCDGs), which can reach lower metallicities in their interstellar mediums (ISMs), as it is the case of I Zw 18. This BCDG has the lowest nebular Oxygen abundance among star-forming galaxies in the nearby Universe, with $Z \sim 1/50\,Z_\odot$ (Aloisi et al. 2007).

Understanding the chemical evolution of dwarf galaxies is essential to constrain models of galaxy formation and evolution, since the fraction of heavy elements within a galaxy is not only related to secular processes but can also carry imprints of past merging episodes (Lequeux et al. 1979; Skillman, Kennicutt & Hodge 1989;

Croxall et al. 2009). The mass–metallicity relation is a widely studied empirical trend that holds from dwarfs to very massive galaxies, where the most massive galaxies are also more metal rich (Rubin, Ford & Whitmore 1984; Pilyugin & Ferrini 2000; Tremonti et al. 2004; Andrews & Martini 2013). An explanation for this relation is the easier retention of the metallic content by galaxies with deeper gravitational potential wells, since the mechanisms of gas transport such as gas accretion (infall) and winds (outflows), which are able to affect the metallicity of a galaxy, depend on the mass of the system (Gibson & Matteucci 1997; Dalcanton 2007). Thus, dwarf galaxies are excellent laboratories to study the chemical evolution of metal-deficient galaxies and offer unique conditions to improve our understanding of galaxy formation and evolution.

In this paper, we analyse an intriguing object in the vicinity of the massive early-type galaxy (ETG) Mrk 1172. This object has available photometric data in the optical (Sloan Digital Sky Survey, SDSS) and in the NUV and FUV (Galaxy Evolution Explorer, *GALEX*), but, to the best of our knowledge, has no previous detailed analysis on the literature (see Section 2.2). In Section 2, we introduce the data and the adopted analysis methodologies. In Section 3, we briefly describe the techniques and present the results obtained. In Section 4, we discuss our results and the conclusions are presented in Section 5. Throughout this work, we adopt $H_0 = 69.32 \, \mathrm{km \, s^{-1} \, Mpc^{-1}}$, $\Omega_\mathrm{m} = 0.2865$, $\Omega_\Lambda = 0.7135$ (Hinshaw et al. 2013), and oxygen abundance as a tracer of the overall gas phase metallicity, using the two terms interchangeably, and a solar oxygen abundance of $\log(\mathrm{O/H}) + 12 = 8.76$ (Steffen et al. 2015).

2 OBSERVATIONS AND DATA REDUCTION

In this work, we present integral field spectroscopy (IFS) of the Mrk 1172 region (J020536.18-081443.23) from Program-ID 099.B-0411(A) (PI: Johnston). The data were obtained using the Multi-Unit Spectroscopic Explorer (MUSE; Bacon et al. 2010) on the Very Large Telescope (VLT) in the wide-field mode (WFM), covering the nominal wavelength range of 4650–9300 Å with mean spectral sampling of 1.25 Å, a field of view (FoV) of 1x1 arcmin², angular sampling of 0.2 arcsec and seeing of ∼1.4 arcsec. Mrk 1172 was observed on the nights of 2018 August 10 and 2018 October 1, with a total exposure time of 1.6 h split over six exposures. The images were rotated and offset to remove the effect of slicers and channels.

2.1 Data reduction

For each night of observations a standard star was observed for flux and telluric calibrations, sky flats were taken within a week of the observations and an internal lamp flat was taken immediately before or after each set of observations. This lamp flat image was used to correct for the time- and temperature-dependent variations in the background flux level of each CCD. Additional bias, flat-field, and arc images were observed the morning after each set of observations.

The data were reduced using the ESO MUSE pipeline (Weilbacher et al. 2020) within the ESO Recipe Execution Tool (ESOREX) environment (ESO CPL Development Team 2015). First, we created master bias and flat-field images and a wavelength solution for each detector and for each night of observations. The flux calibration solution obtained from the standard star observations and the sky flats were then applied to the science frames as part of the post-processing steps. The reduced pixel tables created for each exposure by the post-processing steps were combined to produce final data cube. Since the sky-subtraction applied as part of the EsoRex pipeline leaves behind significant residuals that may contaminate the spectra

of faint sources, particularly at the NIR wavelengths, we applied the Zurich Atmosphere Purge (ZAP; Soto et al. 2016) to the final data cube in order to improve sky subtraction and minimize these artefacts.

2.2 Data specifications

During the inspection the data cubes from the MUSE Program-ID 099.B-0411(A), we identified an extended nebular region in the FoV of the ETG Mrk 1172 ($\alpha = 02^\mathrm{h}05^\mathrm{m}36\overset{\mathrm{s}}{.}19$, $\delta = -08^\mathrm{h}14^\mathrm{m}43\overset{\mathrm{s}}{.}25$). This region occupies a projected area of approximately 92 arcsec² in the observed FoV, calculated by defining a rectangle containing the correspondent object. The FoV is shown in the top left-hand panel of Fig. 1. We inspected this FoV in SDSS, and found that the bright source to the north-east of MRK 1172 (SDSS J020537.54−081411.5) and the two sources to the south (SDSS J020538.07−081501.2 and SDSS J020537.43−081502.2) are stars. The SDSS data also showed many small galaxies around Mrk 1172, most of them not visible in our data, indicating that this system could perhaps be a fossil group. Our object of interest is listed as SDSS J020536.84−081424.7, and has photometric information, though no spectra is available. This object also appears in the GALEX catalogue as GALEX J020536.7−081424, where photometric information on the NUV and FUV is available. For simplification, throughout this paper we will refer to it as the dwarf irregular galaxy (dIGal).

To illustrate the spectra of the dIGal and Mrk 1172, we selected the spaxels with highest SNR in each galaxy, the locations of which are represented by blue crosses in the top left-hand panel of Fig. 1. Both spectra are shown in the right-hand panel of Fig. 1, with main emission and absorption lines labelled. There are two prominent lines in Mrk 1172 spectrum red-wards of the H α absorption line that resemble emission lines. Comparing our spectrum with the one available in SDSS, we notice that these features are absent in the SDSS spectrum. These features are not normal sky lines, since they are broad and do not appear in the spaxels corresponding to sky background. There are other lines that appear in the red part of the spectrum, but curiously they are present only on the data corresponding to the second night of observation. We believe that these features are actually artefacts from the telluric correction. Usually telluric lines appear as broad absorption lines. However, in the case observations from the second night, the telluric lines are stronger in the standard star datacube than in the science datacube, causing an overcorrection of these features, and thus appearing as emission lines in the final datacube.

In the left-hand of panel of Fig. 1, we present the FoV now centred on the wavelength range corresponding to the main emission lines seen in the dIGal spectrum, subtracting the adjacent continuum. The emission lines and the continuum regions used in Fig. 1 are listed below:

(i) H α + [N II]: 6525–6535 Å, 6590–6600 Å
(ii) [O III] λ5007: 4990–5000 Å, 5015–5044 Å
(iii) [S II] : 6650–6700 Å, 6800–6900 Å

Using the strong emission lines in the spectra of the dIGal, we were able to measure its redshift as $z = 0.04025 \pm 0.00003$. In SDSS, Mrk 1172 has a reported redshift of $z = 0.04115$ (Ahn et al. 2012). The redshift measured for Mrk 1172 with MUSE observations is consistent with this previous measurement, and this is the value used throughout the paper.
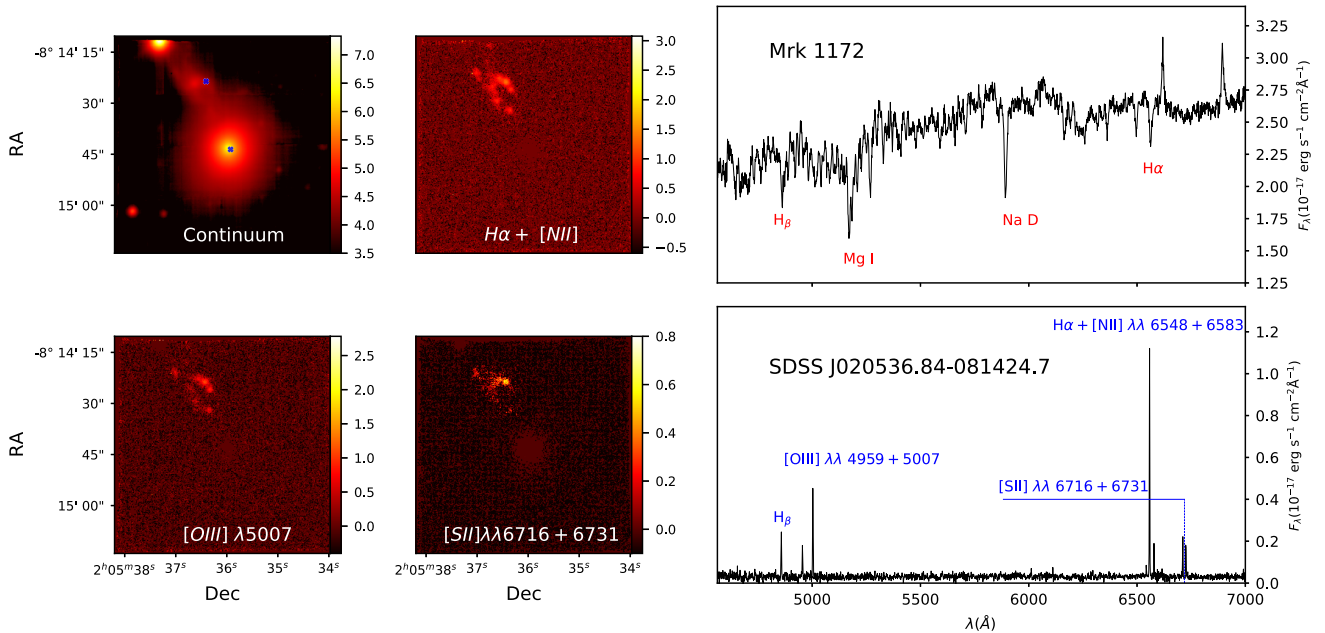
Figure 1. The MUSE FoV continuum centred in Mrk 1172 (top left), $H\alpha + [N\,\textsc{ii}]\lambda\lambda 6550 + 6585$ (top central), $[O\,\textsc{iii}]\lambda 5007$ (bottom left), and $[S\,\textsc{ii}]\lambda\lambda 6716 + 6731$ (bottom central) wavelength ranges. The wavelength windows used to subtract the continuum from the flux of each emission lines are presented in Section 2. The spectrum of Mrk 1172 highest SNR spaxel is presented in top right-hand panel, while in bottom right-hand panel we present the spectrum for the highest SNR spaxel for the dIGal. The location of these spaxels within the FoV is indicated in blue in the top left-hand panel. The colourbars represent in logarithmic scale the flux in each image, in units of $10^{-20}\,\mathrm{erg\,s^{-1}\,cm^{-2}}$.

3 ANALYSIS

3.1 Stellar population fitting

A spatially resolved stellar population synthesis analysis is essential to reveal information regarding the formation, evolution and current state of the observed systems. With such techniques we can obtain the star-formation history (SFH) of both Mrk 1172 and the dIGal, as well as separating the stellar continuum/absorption features and the emission lines from the gas. This analysis will allow us to estimate several properties of the galaxies, such as extinction, SFR and other properties that shall be discussed further, and which can be illustrated via 2D maps (Cid Fernandes et al. 2013; Mallmann et al. 2018; do Nascimento et al. 2019).

To perform the stellar population synthesis we use the MEGACUBE module, which was developed to work as a front-end for the STARLIGHT code, operating in three main modules (Cid Fernandes et al. 2005; Mallmann et al. 2018; Riffel et al. 2021). Since STARLIGHT is designed to operate with ASCII-format files, the spectrum of each spaxel needs to be extracted from the original *fits* files, applying several pre-processing corrections, i.e. rest-frame spectrum shifting and galactic extinction correction. We used the dust maps from Schlegel, Finkbeiner & Davis (1998) and the CCM reddening extinction law (using $R_V = 3.1$, Cardelli, Clayton & Mathis 1989; O'Donnell 1994).

In order to increase the SNR of the individual spaxels, we have binned the original data cube 2x2 along the spatial direction. In order to increase the SNR of the individual spaxels, we have binned the original data cube 2x2 along the spatial direction. Since the spatial coverage of MUSE is large, many spaxels within the FoV cover empty regions in the sky or correspond to objects in the FoV that we would like to mask out from the analysis, such as stars. Therefore, it is useful to create a 2D boolean mask to flag valid and invalid spaxels. However, to create the mask we must adopt a reliable criteria to separate valid spaxels from the invalid ones. In this work, we adopt the following criteria:

(i) The flux vector of the individual spaxel must present 5 per cent or lower of negative and infinite numbers within the array in order to avoid the noisy spaxels, especially from the edges. In the case of spaxels considered to be valid by the above criterion but that still have few invalid numbers, we replace this numbers by applying an interpolation with neighbouring valid values.

(ii) The maximum of the flux (emission or absorption lines) must be at least 1.5 times greater than the standard deviation for that flux vector. In this way only spaxels with high SNR and/or strong emission and absorption lines are set as valid.

The values used to create the criteria were obtained after several tests, for example by comparing the final 2D mask with the continuum image added with Hα emission, as shown in Fig. 2. Finally, each spaxel was convoluted with a Gaussian function[1] in order to match the spectral resolution of the target spectra ($R \sim 2850$ at 7000Å) with that of the simple stellar population (SSP) models [which have a full width at half-maximum (FWHM) = 2.51 Å resolution (Vazdekis et al. 2010, 2016)] and rebinned them to $\delta\lambda$ = 1 Å. For the spaxel meeting, the above criteria and with the corrections applied we performed the stellar population synthesis. We used the Granada-Miles SSP models computed with the PADOVA200 isochrones and Salpeter IMF (Vazdekis et al. 2010; Cid Fernandes et al. 2014). We adopted 21 ages (0.001, 0.0056, 0.01, 0.014, 0.020, 0.031, 0.056,

---

[1]The new Gaussian kernel was obtained by subtracting the data and model σ values in quadrature and taking its root square mean value.
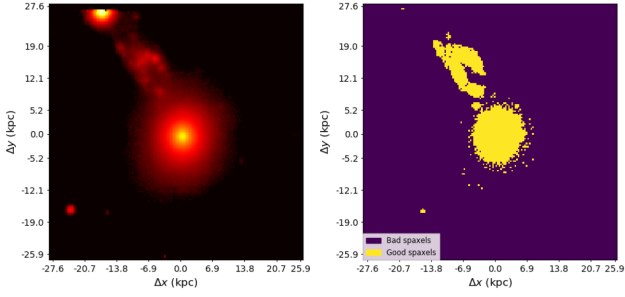
Figure 2. Comparison between Mrk 1172 FoV in continuum plus H α emission (left-hand panel) with a binary map (left-hand panel), where the yellow regions represent the spaxels used in the synthesis, while the purple spaxels are discarded. Undesired high SNR spaxels, such as those corresponding to the stars in the FoV were masked manually. The coordinates presented represent the offset in kpc from the reference spaxel of the FoV, centred in Mrk 1172.

0.1, 0.2, 0.316, 0.398, 0.501, 0.638, 0.708, 0.794, 0.891, 1, 2, 5, 8.9, and 12.6 Gyr) and four metallicities (0.19, 0.39, 1.0 and 1.7 $Z_\odot$). The fit was performed in the 4800–6900 Å spectral range with the normalization point at $\lambda_0 = 5600$ Å, a spectral region free of absorption/emission lines. The prominent lines present in Mrk 1172 spectra do not interfere in the stellar population synthesis, since they were masked out. For safety, we also used the sigma clipping algorithm of STARLIGHT in order to remove any additional spurious features (see Fig. 3).

With the stellar population synthesis done, we inspect the result for individual spaxels in Mrk 1172 and the dIGal. The locations of the spaxels with the highest SNR (approximately 90 and 7, respectively) spaxels in each target are marked in blue in Fig. 1. In Fig. 3, we show examples fits to these spectra, with Mrk 1172 in the top panels

and for the dIGal in the bottom panels. We present the observed spectrum in black with the best-fitting synthetic spectrum in red, and below we show the residual spectrum and the regions masked by the sigma clipping method from STARLIGHT for both cases. In the right-hand panels, we show the histograms of the contribution weighted by luminosity of each stellar population with its respective ages. Mrk 1172 has dominant old stellar populations ($\sim 10^{10}$ yr), with the contribution of an artificial young stellar population ($\sim 10^7$ yr) that appears due to the AGN in this galaxy (Cid Fernandes et al. 2005; Riffel et al. 2009). Meanwhile, the dIGal is predominantly young, presenting two dominant stellar populations with ages between ~ 100 Myr and ~ 1 Gyr.

The luminosity-weighted mean age ($<t_L>$) for each spaxel can be obtained using (Cid Fernandes et al. 2005):

$$< t_L >= \sum_j a_j \log t_j, \tag{1}$$

where t_j is the age of the jth SSP model spectrum, and a_j is a normalization factor that takes into account the fact that the sum of the SSPs used to reproduce the input spectrum is not necessarily 100 per cent (Cid Fernandes et al. 2005). The resulting map is presented in Fig. 4, showing that the dIGal is dominated by young and intermediate stellar populations, while Mrk 1172 is dominated by old stellar populations. This figure shows the spatial distribution of the information, given by the histogram in Fig. 3. It can be seen in Fig. 4 that the stellar populations dominating the light emitted from the dIGal are considerably younger than those in Mrk 1172.

3.2 Fitting of the emission-line profiles

Having fitted the underlying spectrum of each spaxel, we subtract it from our observed data, resulting in pure emission line spectra. No
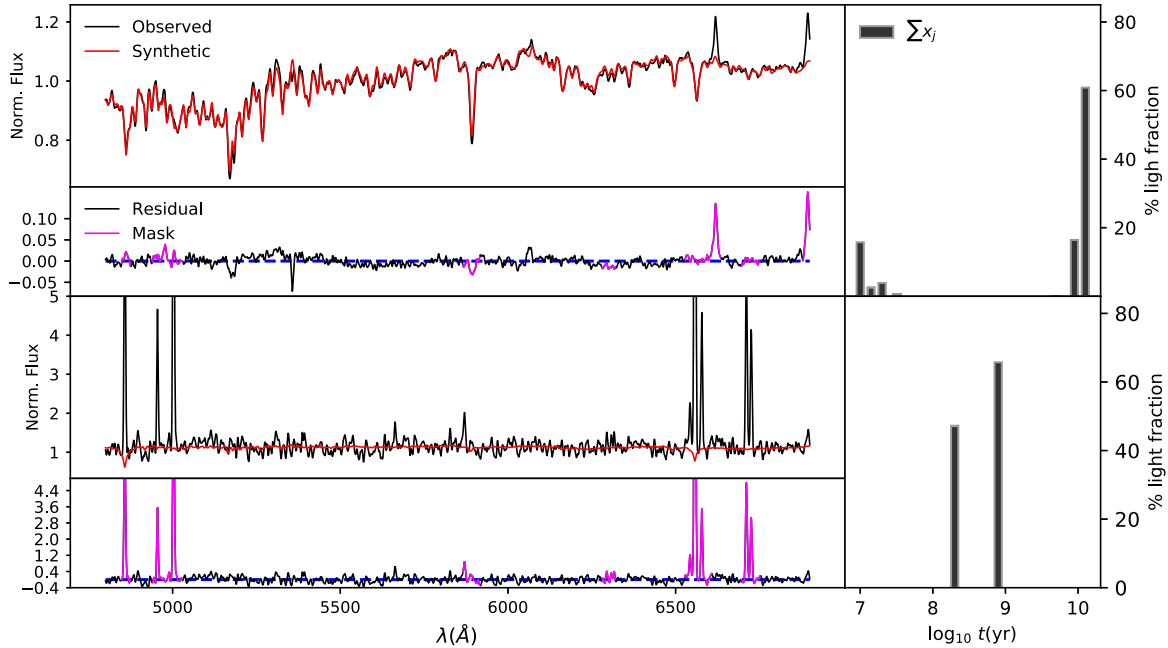

Figure 3. Synthesis results for the highest SNR spaxel for Mrk 1172 and the dIGal. *Top left-hand panel*: In black, the observed spectrum of Mrk 1172, where the flux is normalized using $F(\lambda_0)$. In red, the synthetic spectrum (the best fit from the stellar population synthesis). *Second top left-hand panel:* Residual spectrum for Mrk 1172 in black, with the regions masked by sigma clipping method in magenta. At the bottom left-hand panels, the same for the dIGal. *Top right-hand panel*: Histogram presenting the luminosity-weighted contribution of each stellar population for Mrk 1172 best fit and their ages. At the bottom right-hand panels, the same for the dIGal.
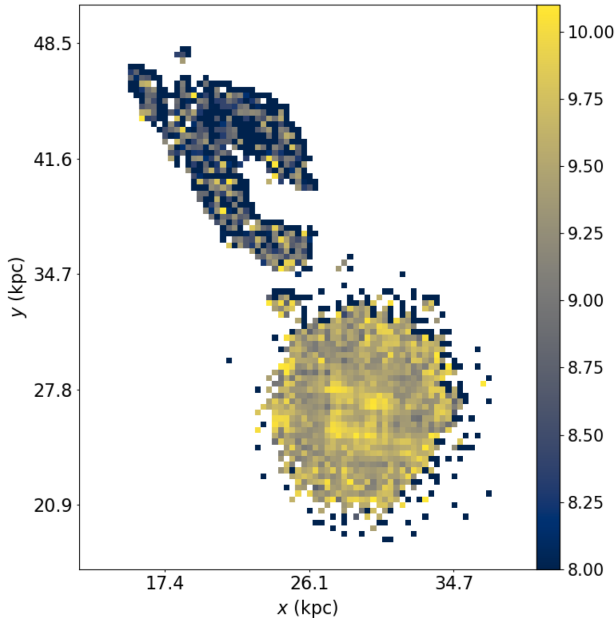
Figure 4. Mean luminosity-weighted age map for Mrk 1172 and the dIGal in Gyr, obtained via spatially resolved stellar population synthesis.

emission lines were detected in locations corresponding to Mrk 1172, while strong emission features were found in the spectra of the dIGal, as seen in Fig. 1. We measured the fluxes using the IFSCUBE (Ruschel-Dutra & de Oliveira 2020) tool, which fits the emission-line profiles at each position by single Gaussian curves.

3.2.1 Single Gaussian fitting

Fig. 3 shows that the synthetic spectrum produced through the stellar population synthesis models the continuum very well, thus we have not added a polynomial function to fit the continuum. The fitting of the emission lines was performed on the residual cube, obtained by the subtraction of the modelled continuum/absorption spectra from the cube used in the stellar population synthesis (i.e. a rest-frame spectrum, resampled in $\Delta\lambda = 1$ Å and corrected for Galactic reddening). As a first approach, we assume that emission lines corresponding to transitions on the same atom (i.e. [O III] $\lambda4959$ and [O III] $\lambda5007$) belong to the same kinematic group.[2] Since the strongest emission lines in the spectrum of the dIGal are from transitions of H, O, N and S, we use four different kinematic groups, one for each element. We also used specific constraints for the line ratios, e.g. [N II] $\lambda6583$ $= 3.06 \times$ [N II] $\lambda6548$ and $0.4 <$ [S II]λ 6717/[S II]λ $6731 < 1.4$ (Osterbrock & Ferland 2006). The ratio of [O III] emission lines was kept free of constraints during the fitting process.

Fig. 5 shows an example of the outcomes of this fitting procedure, where we present the spectral regions containing the fitted emission lines. The observed spectrum is shown as a solid black line, the stellar continuum is shown in the solid blue lines and the best-fitting model

---

[2]Many spectral features are physically linked, being produced in the same region of the target of study. Therefore, it is reasonable to assume that different transitions of the same atom were produced in the same region, and their emission lines share properties like velocity and velocity dispersion. When both lines share these properties, we say that they belong to the same kinematic group.
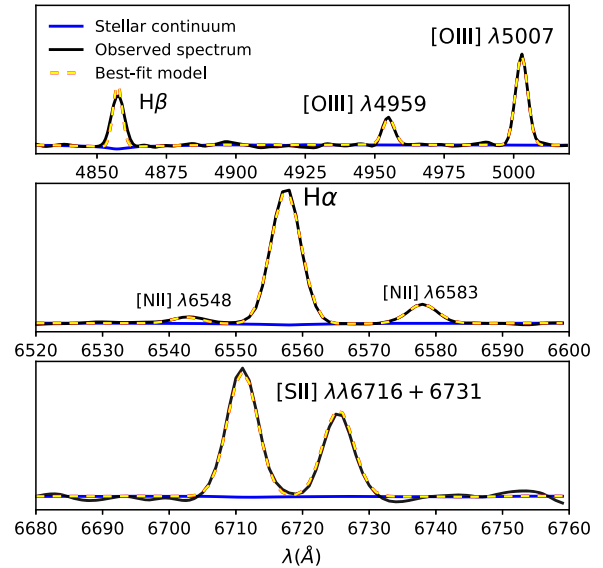
Figure 5. Emission lines in the dIGal spectrum fitted using Gaussian profiles with IFSCUBE. In black, the observed spectrum, in blue the continuum, and the dashed yellow line represents the model fit.

is represented by a dashed yellow line. Besides fluxes, IFSCUBE also provides the gas kinematic parameters (gas velocity and velocity dispersion). In the next sections, we analyse these quantities.

An important side note is that the S doublet, which can be used to estimate the electron gas density (n_e, Osterbrock & Ferland 2006; Ryden & Pogge 2021), presents an emission line ratio that falls in the limit of sensibility of the density relation for the dIGal, making it impossible to determine n_e with accuracy. Therefore, we have assumed the lower limit of $n_e \sim 100$ cm^{-3} for the galaxy in the following analysis.

3.2.2 Gas excitation

The emission-line ratios allow us to determine the nature of the ionization source of the gas in the dIGal. For this analysis, we used the traditional BPT diagnostic diagram (Baldwin, Phillips & Terlevich 1981) to create spatially resolved maps of the likely ionization sources (for a similar analysis see Wylezalek et al. 2017; do Nascimento et al. 2019). In Fig. 6, we show these maps for the dIGal. In the diagram involving the lines ratios [N II]/H α *versus* [O III]/H β (top left-hand panel) the solid blue line separating H II from the transition region, as well as the solid red line separating Seyfert and LINER regions were taken from Kauffmann et al. (2003). The solid green line separating transition region from the AGN region was obtained from Kewley et al. (2001). The symbols are the positions of individual spaxels in the diagnostic diagram and the spatial distribution within the galaxy is shown on the right-hand panel. For the diagram involving [S II]/H α *versus* [O III]/H β line ratios (left bottom) the solid magenta line is from Kewley et al. (2001), while the solid red line is from Kewley et al. (2006).

Both diagrams show that the gas is ionized by young massive stars rather than by an AGN. Ionization by shocks are investigated using the fast radiative shock models from Allen et al. (2008), adopting solar metallicity, $n_e = 100$ cm^{-3}, and varying the values of magnetic field. With an inspection of the curves of emission line ratio versus shock velocity, we observe that the values for the gas in the dIGal are coherent to shock velocities <100 km s^{-1}. In the regime of such
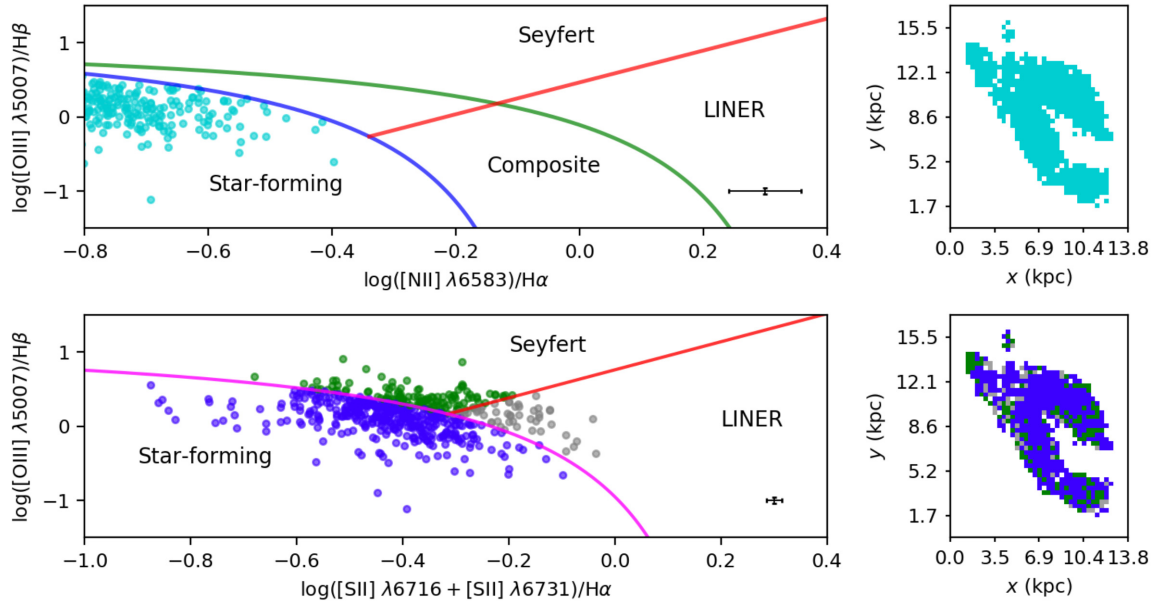
Figure 6. Spatially resolved diagnostic diagram for the dIGal. *Top left-hand panel:* The circles represent the position of individual spaxels in the diagnostic diagram. The relations for the solid blue and red lines were taken from Kauffmann et al. (2003). The relation for the solid green line was obtained from Kewley et al. (2001). *Bottom left-hand panel*: Same as top left-hand panel, now using different emission line ratio for the diagram. The red and magenta solid lines are given by Kewley et al. (2006) and Kewley et al. (2001), respectively. *Top/bottom right-hand panel*: The dIGal with each spaxel coloured corresponding to its position in the diagnostic diagram. The bars in the bottom right-hand corner of the right-hand panels indicate the mean error associated with the position of each point in the diagram.

low velocities, it is unlikely for shock ionization to be the dominant mechanism of photoionization in the dIGal.

3.3 Extinction

We have already corrected the observed spectra for the Galactic dust extinction using the Schlegel et al. (1998) dust maps, but the intrinsic attenuation of the dIGal still remains, and correcting for this effect is essential for obtaining many of the important properties concerning the gas components.

To perform this correction, we have followed Osterbrock & Ferland (2006). By considering I_λ as the observed intensity for a given wavelength and I_{λ_0} as the intrinsic intensity, we have

$$I_\lambda = I_{\lambda_0} \times 10^{-cf(\lambda)}, \tag{2}$$

where c is an undetermined constant and $f(\lambda)$ is the extinction curve. The number of magnitudes of extinction, A_λ, is related to the lines intensity ratio by

$$A_\lambda = -2.5 \log\left(\frac{I_\lambda}{I_{\lambda_0}}\right). \tag{3}$$

A_λ is related to A_V via the reddening law. By assuming the case B of recombination, with an intrinsic intensity ratio of H α/H β = 2.87, electron temperature of 10^4 K and $R_V = 3.1$, A_V can be derived using

$$A_V = 7.23 \times \log\left[\frac{F(\mathrm{H}\,\alpha)}{F(\mathrm{H}\,\beta)}\right] - 3.31, \tag{}$$

where $F(\mathrm{H}\,\alpha)$ and $F(\mathrm{H}\,\beta)$ are the observed fluxes. This equation represents the attenuation caused by dust and molecular gas surrounding the H II regions. The extinction map produced with this equation for the dIGal is shown in Fig. 7.

3.4 Star formation rate

From the diagnostic diagram one can see that all spaxels of the dIGal are in the star-forming region, so it is interesting to estimate its SFR. We can calculate it using the Balmer recombination lines. Assuming case B of recombination and a Salpeter initial mass function (IMF), we can use the expression below to estimate the instantaneous SFR of the dIGal (Kennicutt 1998):

$$\mathrm{SFR}(\mathrm{M}_\odot\ \mathrm{yr}^{-1}) = 7.9 \times 10^{-42} L(\mathrm{H}\,\alpha)\ (\mathrm{erg\ s}^{-1}). \tag{4}$$

The luminosity $L(\mathrm{H}\,\alpha)$ was obtained from the flux of H α emission line using the distance of the dIGal, which was derived from its redshift of $z = 0.04025 \pm 0.00003$. Fig. 8 shows the resulting SFR map. The colourbar shows the SFR in units of $10^{-3}\ \mathrm{M}_\odot\ \mathrm{yr}^{-1}$. Integrating the SFR over all spaxels results in a total SFR of 0.70 M$_\odot$ yr^{-1} and a ΣSFR of $1.4 \times 10^{-2}\ M_\odot$ yr^{-1} kpc^{-2}, which was obtained by dividing the SFR by the area of each spaxel. The peak value for an individual spaxel reaches $6.75 \times 10^{-3}\ \mathrm{M}_\odot$ yr^{-1}.

3.5 Stellar mass

We can use the information acquired with the stellar population synthesis to estimate the current stellar mass $M_\star$[3]:

$$M_\star(\mathrm{M}_\odot) = 4\pi d^2 \times M_{\mathrm{tot}}^{\mathrm{cor}} \times (3.826 \times 10^{33})^{-1}, \tag{5}$$

where d is the distance to the galaxy in units of cm and the base spectra used is in a proper unit of L$_\odot$ Å^{-1}M$_\odot^{-1}$ and the observed spectra in units of erg s^{-1} cm^{-2} Å^{-1}. $M_{\mathrm{tot}}^{\mathrm{cor}}$ is a STARLIGHT output parameter in units of M$_\odot$ erg^{-1} cm^{-2}, which gives the current mass of stars in the galaxy based on the contribution of each SSP to the best-fitting synthetic spectrum. We can apply equation (5) to each spaxel of our

---

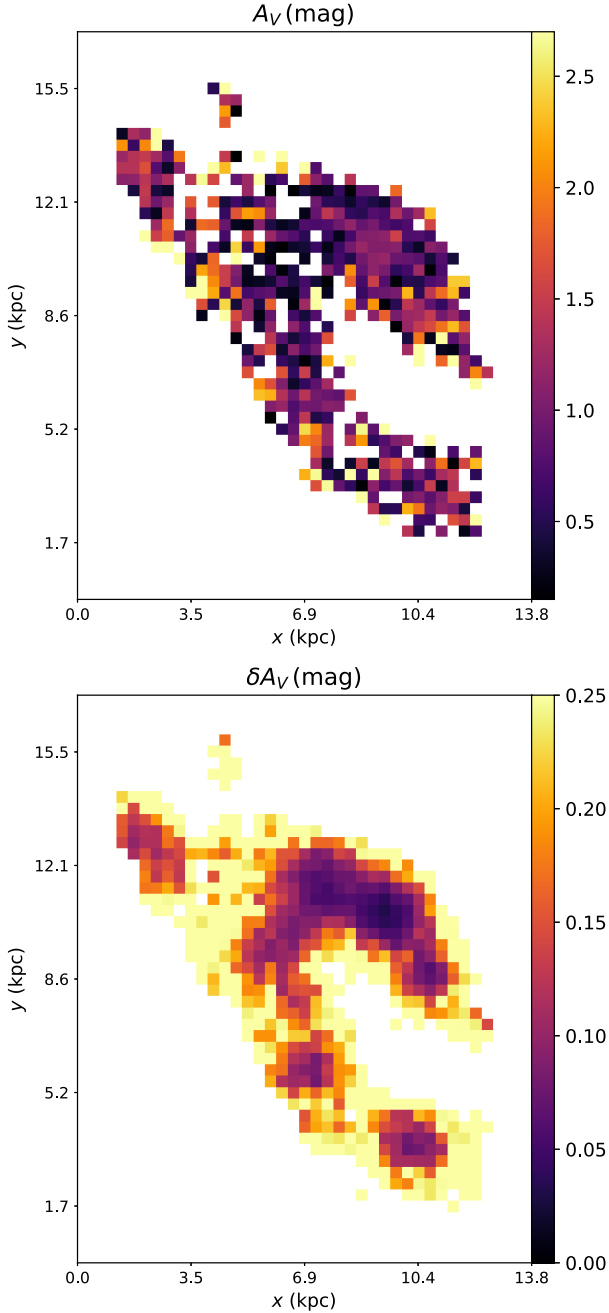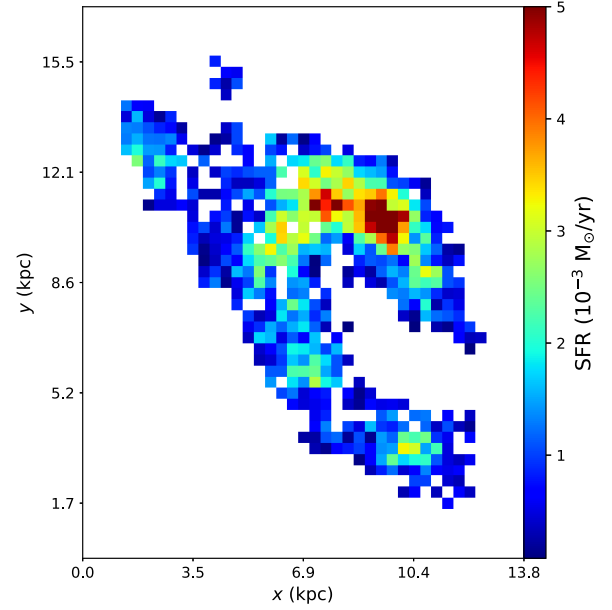[3]https://minerva.ufsc.br/starlight/files/papers/Manual_StCv04.pdf

Figure 8. The dIGal SFR distribution map. Regions with high SFR appear in red, while regions without significant star formation appear in blue. The colourbar indicates the values of SFR associated with each colour in units of $M_\odot \, yr^{-1}$.

where M_{tot}^{ini} represents the mass that has been converted into stars and is given in units of $M_\odot \, erg^{-1} \, cm^{-2}$ (Riffel et al. 2021)[3]. Applying equation (6) to all valid spaxels, we obtain $M_\star^{ini} \sim 1.7 \times 10^{11} M_\odot$ for Mrk 1172 and $M_\star^{ini} \sim 3.9 \times 10^9 M_\odot$ for the dIGal. $M_\star^{ini}$ is expected to be higher than the current stellar mass of the system due to the mass returned to the ISM by SNe and winds.

3.6 Ionized gas mass

Following, for example, do Nascimento et al. (2019), we can calculate the mass of the ionized gas by using the expression:

$$M = n_e m_p V f, \tag{7}$$

where n_e is the electron density of the gas, m_p is the proton mass, V is the volume of the ionized region, and f is the filling factor. Using the emissivity of Hβ ($j_{H\beta}$), we can calculate the total luminosity of this line:

$$L(H\beta) = \int \int j_{H\beta} \, d\Omega dV. \tag{8}$$

We know from Osterbrock & Ferland (2006) that for recombination case B (in the low-density limit), assuming $T = 10^4$ K we have

$$\frac{4\pi j_{H\beta}}{n_e n_p} = 1.24 \times 10^{-25} \, \frac{erg \, cm^3}{s},$$

where n_e and n_p are the electric and proton densities, respectively. Using this result into the integral in equation (8), we obtain $L(H\beta)$ in units of erg s^{-1}:

$$L(H\beta) = 1.23 \times 10^{-25} \, n_e n_p V f.$$

Assuming the gas is completely ionized ($n_e = n_p = n$), we can isolate Vf from the expression above and use it in equation (7). Considering the lower limit of $n_e = 100 \, cm^{-3}$, we obtained the mass of the ionized gas:

$$M(M_\odot) = 6.782 \times 10^{-35} L(H\beta), \tag{9}$$

Figure 7. *Top panel*: The extinction map for the dIGal. The lighter regions of the map represent higher light extinction, while the darker regions represent lower extinction. In white, the masked points, excluded from the plot. The colourbar shows the range of extinction values measured in the region in magnitude units. *Bottom panel*: Map with the uncertainties of the A_v measurement, represented by δA_v, where we observe that the uncertainties drop as the spaxel is closer to the edge of the dIGal.

datacube to obtain the total stellar mass for both Mrk 1172 and the dIGal. We obtain $M_\star \sim 1.2 \times 10^{11} M_\odot$ for Mrk 1172 and $M_\star \sim 3.0 \times 10^9 M_\odot$ for the dIGal. Similarly, we can estimate how many solar masses have been processed into stars through the lifetime of the system $(M_\star^{ini})^3$ by using

$$M_\star^{ini} \, (M_\odot) = 4\pi d^2 \times M_{tot}^{ini} \times (3.826 \times 10^{33})^{-1}, \tag{6}$$

where $L(H\beta)$ is the luminosity of Hβ emission line, in units of erg s^{-1}. Since we used $n_e = 100\,cm^{-3}$, the mass resulting from equation (9) should be interpreted as a lower limit mass. We applied equation (9) to the dIGal, where Hβ is strong for the majority of the spaxels in the region, by using the reddening corrected $F(H\beta)$ to calculate $L(H\beta)$ for each spaxel in the dIGal. Integrating over the whole region corresponding to the dIGal, we have obtained $M = 3.8 \times 10^5 M_\odot$ for the ionised gas mass.

3.7 Oxygen abundances

We aim to characterize the dIGal with respect to metallicity, using as proxy the oxygen abundance in its ISM. Since we are not able to directly measure the electron temperature (T_e) because the [O III]λ4363 Å emission line is out of our observed region we cannot use the direct method (e.g. Osterbrock & Ferland 2006). However, many calibrations were made in the past decades without the need of T_e determination (e.g. Pettini & Pagel 2004; Nagao, Maiolino & Marconi 2006; Pérez-Montero & Contini 2009; Marino et al. 2013; known as indirect methods). Useful calibrations are given in Marino et al. (2013):

$$\log(O/H) + 12 = 8.533(\pm0.012)$$
$$- 0.214(\pm0.012) \times O3N2, \tag{10}$$

$$\log(O/H) + 12 = 8.743(\pm0.027)$$
$$+ 0.462(\pm0.024) \times N2, \tag{11}$$

where O3N2 and N2 indices are defined as follows (Alloin et al. 1979; Storchi-Bergmann, Calzetti & Kinney 1994):

$$O3N2 = \log\left(\frac{[O\,III]\lambda5007}{H\beta} \times \frac{H\alpha}{[N\,II]\lambda6583}\right), \tag{12}$$

$$N2 = \log\left(\frac{[N\,II]\lambda6583}{H\alpha}\right). \tag{13}$$

The ionization parameter in galaxies between $0 < z < 0.6$ changes such that the line ratios [O III]/Hβ and [N II]/Hα from giant low-surface brightness H II regions begin to rise and lower, respectively. When using a metallicity tracer for galaxies in that redshift range is crucial either to take into consideration the behaviour of the ionization parameter and the change in the emission-line ratios or to use a tracer that is independent of the conditions of ionization of the ISM (Monreal-Ibero et al. 2011; Kewley et al. 2015). With this in mind, we used a calibration based on [N II] and [S II] in addition to the previous calibrations, given by Dopita et al. (2016):

$$\log(O/H) + 12 = 8.77 + \log([N\,II]/[S\,II]) + 0.264$$
$$\times \log([N\,II]/H\alpha). \tag{14}$$

These calibrations were applied to each spaxel of the dIGal, producing three Oxygen abundance maps, two for each tracer of Marino et al. (2013) and the third for the calibration from Dopita et al. (2016). These are shown in Fig. 9. In the first two cases, we obtain values in the range of $8.0 < \log(O/H) + 12 < 8.6$, which represents a range of approximately $0.2\,Z_\odot < Z < 0.7\,Z_\odot$. In the third case, the metallicity spans a wider range of $7.5 < \log(O/H) + 12 < 8.5$ (i.e. $0.05\,Z_\odot < Z < 0.5\,Z_\odot$). To have a representative value, we calculated the average metallicity for each map. We have obtained $\log(O/H) + 12 = 8.28 \pm 0.03$ for the O3N2 index and $\log(O/H) + 12 = 8.296 \pm 0.004$ for the N2 index. For the calibration given in Dopita et al. (2016), we obtained $\log(O/H) + 12 = 8.2 \pm 0.2$. As a sanity check, we have calculated the abundance derived from

the emission lines measured in an integrated spectrum of the dIGal, and the values are consistent.

3.8 Kinematics

There are many intriguing aspects of the dIGal: its irregular morphology, its proximity to Mrk 1172 and its physical properties that indicate it may be interacting with Mrk 1172. Thus it is important to explore the kinematics of the dIGal. We can obtain the radial velocity, v, of the gas for the identified emission lines in the dIGal spectra directly from IFSCUBE single Gaussian fit, as well as the velocity dispersion, σ. In the fit process, we fixed the doublets as being in the same kinematic group, meaning that the resulting velocity values will be the same for the same ion. In Fig. 10, we show both velocity, corrected by subtracting off the mean velocity of the system, and velocity dispersion (σ) maps for Hα, [O III]λ5007, [N II]λ6548, and [S II]λ6731 emission lines.

First we observe, especially in the maps of centroid velocity, that the gradient seen is more smooth in the case of Hα emission-line maps. This is due to the fact that in spaxels near the edge of the dIGal (which was defined using the strongest emission line in its spectra, i.e. Hα) the SNR is low and the measurement of emission lines other than Hα have higher uncertainties. Even so, all velocity maps exhibit the same trend for the motion of the gas, where the upper part of the galaxy is moving away from us while the bottom is approaching. Since we do not know the distances with precision, we cannot determine the orientation of the motion of the dwarf galaxy around the ETG.

The maps of velocity dispersion of the gas seem to replicate the trend seen in the maps of radial velocity. In the case of the kinematical group corresponding to the emission lines of [O III], we observe that more spaxels reach values of $\sigma < 90\,km\,s^{-1}$ in comparison to the other maps. Such a difference could be caused, for instance, if this zone of ionization is closer to the region with higher flux of ionizing photons in comparison to the other zones of ionization and being strongly affected by the winds of massive stars. However this difference rarely becomes larger than $20\,km\,s^{-1}$, as can be observed in Fig. 10, and the most likely is that it is not significant. To determine the zero-point in the velocity scale of Fig. 10, we used the rest-frame velocity, calculated using the integrated spectrum of the dIGal. The values of velocity dispersion were corrected by instrumental width, assuming a resolving power R of 1750 at $\lambda \sim 5000$ Å and $R \approx 2500$ at $\lambda \sim 6500$ Å.

Although we do not have information about the gas of Mrk 1172, we can explore its stellar kinematics using the results obtained in the stellar population synthesis. In Fig. 11 we present, in the top left-hand panel, the stellar velocity field for the ETG. To better understand the interaction between both galaxies, we used an analytical model that assumes that the gas has circular orbits around the plane of a disc (van der Kruit & Allen 1978; Bertola et al. 1991). For this model, we used the stellar velocity field of Mrk 1172 and the gas velocity field measured from Hα shown in Fig. 10 and shown in bottom left-hand panel of Fig. 11. The equation that gives the model velocity field is given by

$$V(R, \Psi) = v_s$$
$$+ \frac{AR\cos(\Psi - \Psi_0)\sin(i)\cos^p(i)}{\{R^2[\sin^2(\Psi - \Psi_0) + \cos^2(i)\cos^2(\Psi - \Psi_0)] + C_0^2\cos^2(i)\}^{p/2}},$$

where R is the radial distance to the nucleus projected in the plane of the sky with a corresponding position angle Ψ, v_s is the systemic velocity of the analysed galaxy, A is the velocity amplitude, Ψ_0 is the position angle of the line of nodes, C_0 is a concentration parameter defined as the radius where the rotation curve reaches 70 per cent of
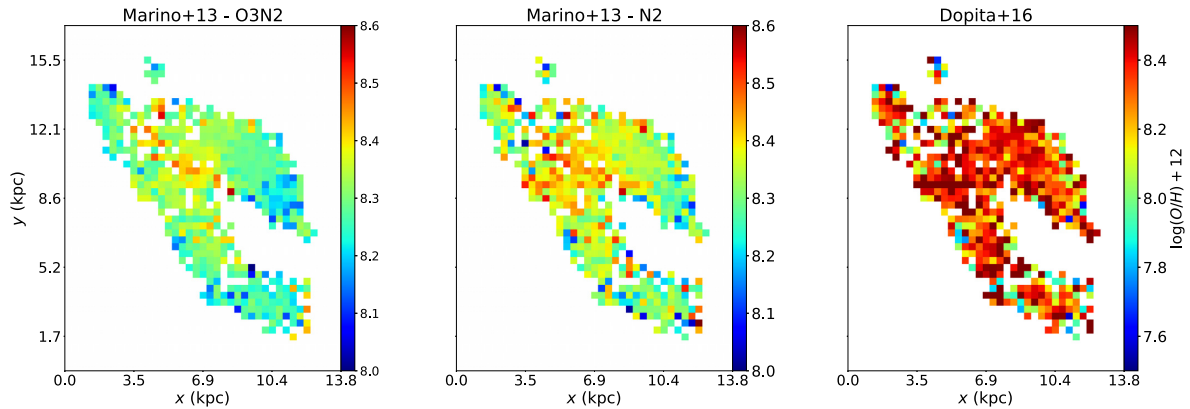
Figure 9. Maps for oxygen abundance obtained using the indirect method, in units of $\log(O/H) + 12$. In left and central panels, the results using O3N2 and M2 indexes from Marino et al. (2013). In right-hand panel, the result using the calibration from Dopita et al. (2016).
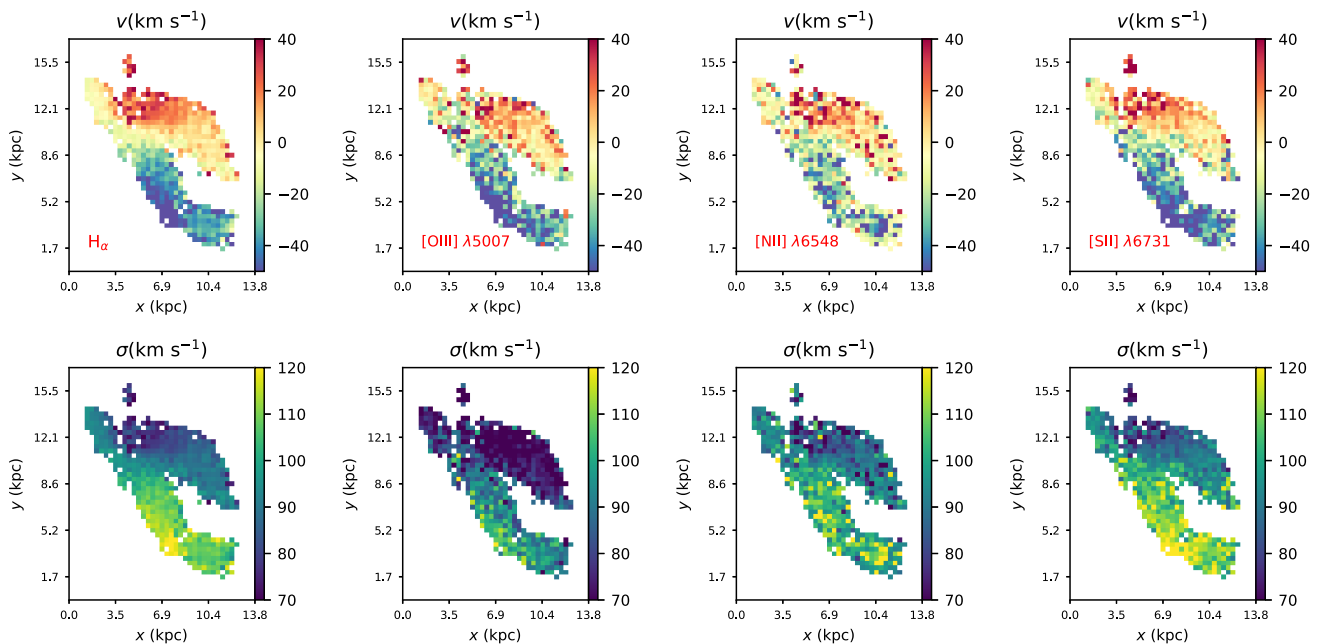

Figure 10. Kinematic maps for H α, [O III]λ 5007, [N II]λ 6548, and [S II]λ 6731 emission lines. In the upper panel, radial velocity maps, and in the lower panel, the turbulence of the gas. Both parameters are obtained from a single Gaussian used to fit the observed emission lines using IFSCUBE.

the velocity amplitude and i is the disc inclination in relation to the plane of the sky. The parameter p varies from 1.0 to 1.5. In Table 1, we summarize the results obtained for the fit. The values of v_s presented were obtained by adding the heliocentric velocity of each galaxy. The residual maps of the fit are presented in the right-hand panel of Fig. 11.

4 DISCUSSION

One important question that arises at this point is: *what is the origin and nature of the nebular emission region identified throughout this paper as the dIGaland how is it connected to ETG Mrk 1172?* In this section, we will use the results presented previously to build possible scenarios for the observed system.

From the stellar population analysis, it is clear that Mrk 1172 and the dIGal do not share similar SFHs. While the ETG is dominated by an old stellar population with no signs of ionised gas, the

dIGal presents a rich emission-line spectra with its stellar emission dominated by very young stellar populations ($t < 10^9$, see Figs 3 and 4). It is worthwhile mentioning that although Fig. 3 displays information for individual spaxels, the results are representative of all the spaxels in each system, and arguments based on this figure can be extended to the entirety of both systems. In Fig. 3, we also observe a significant contribution of very young stellar populations ($t < 10^8$ yr) in the spectra of Mrk 1172. These are probably artificial stellar populations caused by (i) the presence of an AGN in Mrk 1172 or (ii) the absence of blue horizontal branch stars in the models, forcing a young population to take into account the blue light of these stars in the ETG (Cid Fernandes & González Delgado 2010; González Delgado & Cid Fernandes 2010).

An interesting parameter to explore is the magnitude in the *B* band, since it probes the young stellar populations in the galaxy. Although we lack the spectral range to measure the *B*-band magnitude by integrating the spectra, we can use the photometric values of SDSS
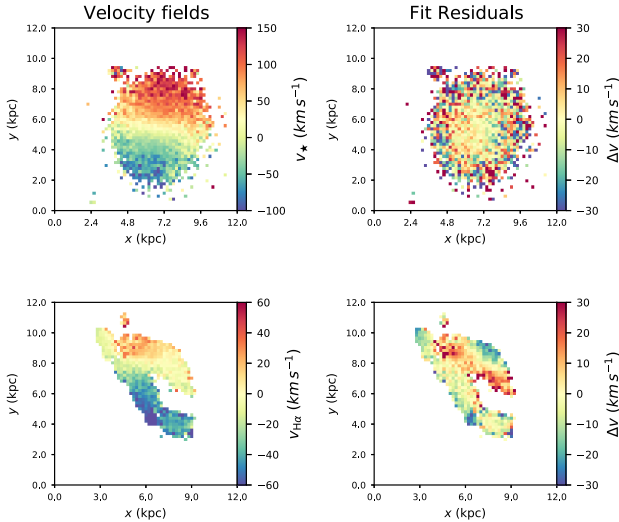
Figure 11. Top left-hand panel: Stellar velocity field of Mrk 1172. Bottom left-hand panel: Velocity field for the gas in the dIGal measured using H α emission line. The values of velocity were obtained by subtracting the systemic velocity of the galaxy ($v_s = -240$ km s^{-1}) from the centroid velocity obtained previously. Right-hand panels: Residual maps for the model fitted.

Table 1. Final result of the fitting process for both galaxies.

	Mrk 1172	the dIGal
v_s (km s^{-1})	12373 ± 5	11835 ± 3
A (km s^{-1})	720 ± 180	310 ± 97
i (°)	30 ± 9	28 ± 10
C_0 (arcsec)	4.8 ± 0.5	4.0 ± 0.9
Ψ_0 (°)	167 ± 4	165 ± 4
p	1.5	1.5

to convert to *B* band using (Jordi, Grebel & Ammon 2006)

$$B - g = (0.349 \pm 0.009)(g - r) + (0.245 \pm 0.006). \quad (15)$$

From SDSS, we have the magnitudes of dIGal: $u = 22.81 \pm 0.52$, $g = 20.65 \pm 0.04$, $r = 20.19 \pm 0.04$, $i = 19.70 \pm 0.04$, and $z = 19.69 \pm 0.11$. By applying equation (15), we obtain $B = 21.00 \pm 0.37$, which corresponds to an absolute magnitude of $M_B \sim -15$ mag, which means the observed dwarf galaxy is faint in the blue band.

We also wish to understand the mechanism responsible for the gas excitation, evidenced by the strong emission lines observed in the dIGal spectra. From the BPT diagnostic diagrams shown in Fig. 6, it is clear that the gas within the dIGal is excited by young hot stars rather than by a hard radiation field. The few spaxels falling in the Seyfert region of the diagnostic diagram are located at the edges of the galaxy and have low SNR, as indicated by the transparency of the circles. We compared our line ratios with predictions of shock models from Allen et al. (2008) and concluded that fast radiative shocks are unlikely to be a significant mechanism of ionization of the gas in the dIGal.

Due to the presence of young stellar populations and the excitation mechanism of the gas, we can say that the dIGal is forming stars, although the efficiency of the process is unknown. The young stars that are ionizing the gas seem to be located in a few clumpy knots along the structure of the dIGal, better traced by the SFR map in

Fig. 8. This structure also becomes visible when looking at the H α collapsed image in Fig. 1 and in the continuum H α emission in Fig. 2, and are typical structures formed in regions with active star formation. Using the Balmer decrement, we produced a reddening map for the dIGal, shown in Fig. 7. The mean A_V is 0.9 mag, but in few spaxels this value is up to ∼2.0 mag, reinforcing the inhomogeneity of the medium, or also the uncertainty in the emission-line ratio for these spaxels. The intensities of the emission lines, used through this paper, have been corrected for dust attenuation.

Using the emission-line fluxes, we calculated the instantaneous SFR using equation (4), obtaining an SFR of 0.70 M$_\odot$ yr^{-1}. We also derived the spatial distribution of SFR for the dIGal ($\sum_{SFR}$), resulting in 1.4×10^{-2} M$_\odot$ yr^{-1} kpc^{-2}. Finally, we calculated a lower limit for the mass of ionized gas in the dIGal using the H β emission-line strength, resulting in a mass of 3.8×10^5 M$_\odot$.

From the stellar population synthesis, we obtained an estimate for the stellar mass of both galaxies. We estimate the values of 3.0×10^9 M$_\odot$ for the dIGal and 1.2×10^{11} M$_\odot$ for Mrk 1172. In the case of the latter, the order of magnitude of this value is coherent to what is expected for massive ETG like Mrk 1172, and is in agreement with a previous estimates for the stellar mass for this galaxy (8.91×10^{10} M$_\odot$; Omand, Balogh & Poggianti 2014). On the other hand, the dIGal has an estimated value of stellar mass comparable to dwarf galaxies, like the SMC, for example (6.5×10^9 M$_\odot$; Bekki & Stanimirović 2009).

With the values of stellar mass and SFR, we can estimate the specific star formation rate (sSFR) for the dIGal, which can be compared with a previous value found in the catalogue of Delli Veneri et al. (2019; DV19 throughout this paper), where the sSFR is measured using photometric information for a large sample of galaxies from SDSS DR7. We have obtained a value of log(sSFR) = −9.63, which is considerably different than the log(sSFR) = −10.85 found in DV19. However, these two values were derived using different techniques, and the photometry of the dIGal is flagged as medium quality in DV19, meaning the direct comparison between both values is hard to perform.

As observed before in this work, the dIGal has an irregular shape and lies next in projection to Mrk 1172. Thus, a natural first assumption is that both galaxies are interacting, and the irregular shape of the dIGal could be partially explained by tidal forces. Analysing the available redshift for Mrk 1172 (which is consistent with our determination) and our measurement for the dIGal, one can calculate a distance of approximately 4 Mpc between both galaxies, for which gravitational interactions could be neglected. However, this calculation does not take into account that the shift in the emission lines of the dIGal could be also caused by its motion in relation to Mrk 1172. Considering that Mrk 1172 has a massive halo, it is possible that this halo is populated by faint dwarf galaxies. In this case, the participation of the dIGal in this group of galaxies should not be discarded, and the estimate of 4 Mpc of distance between both galaxies could be incorrect. As an exercise, if we assume 300 km s^{-1} for the group velocity, for example, it would affect the above-mentioned distance estimate by approximately 3 Mpc, i.e. the uncertainty in the distance estimate due to the relative motion of the dwarf galaxy is large.

To investigate deeper the interaction between both galaxies, we fit a model to the stellar velocity field of Mrk 1172 and to the H α velocity field of the dIGal (see Fig. 11). The final results of the fit are listed in Table 1. It can be seen that both galaxies present similar results for the disc inclination and the position angle of the line of the nodes (i and Ψ_0, respectively). Although the presence of a disc in the dIGal is uncertain, the model fit is satisfactory, and this result

indicates that the motion of the gas in the dwarf galaxy is affected by the ETG. These considerations, combined to the irregular shape of the dwarf galaxy, lead us to the conclusion that Mrk 1172 and the dIGal are currently interacting.

Finding a low-metallicity system next to an ETG, as seems to be the case for Mrk 1172 and the dIGal, deserves further investigation. Here, we use oxygen abundance as a tracer for the metallicity of the ISM of the dIGal and we employ the calibrations from Marino et al. (2013) for each spaxel of the dIGal. The average metallicity obtained is $\log(O/H) + 12 = 8.28 \pm 0.03$ for the O3N2 index and $\log(O/H) + 12 = 8.296 \pm 0.004$ for the N2 index. Since O3N2 is based in emission lines both in the blue and red parts of the spectrum and suffers a strong dependence on the ionization parameters for the ISM ionization conditions of the dIGal. Thus, we used the calibration from Dopita et al. (2016), which has no dependence on the ionization parameters of the galaxy, to compare with the previous results. Using this calibration, we obtained an average value of $\log(O/H) + 12 = 8.2 \pm 0.2$. In general, this third calibration gives slightly lower values of metallicity in comparison to the other maps. Combining the values obtained it is possible to estimate that the metallicity of the dIGal is approximately $1/3\ Z_\odot$. The range of metallicities observed in the dIGal is also observed in metal-poor systems such as dwarf irregulars and some BCDGs (Kunth & Östlin 2000; Gil de Paz, Madore & Pevunova 2003). This feature raises another question: *what is the origin of this metal-deficient content?*

Models of galaxy formation in the Lambda cold dark matter (Λ-CDM) context predict the inflow of metal-deficient gas from the cosmic web. Numerical simulations indicate that this gas can trigger star formation in disc galaxies and dwarf galaxies of the Local Universe (Sánchez Almeida et al. 2015). The triggering of a starburst may happen, as the infalling gas gets compressed when it approaches the disc or also it may be accreted and build up the gas mass of the galaxy to eventually give rise to the starburst due to internal instabilities (Dekel, Sari & Ceverino 2009; Ceverino et al. 2016). In many cases, chemical inhomogeneities can be observed in galaxies in the Local Universe, where localized kpc-size starbursts present considerably lower abundances in comparison to the surrounding ISM. The scenario described above is a plausible interpretation for the metallicity drop in these starburst regions. We believe that the origin of the metal deficient gas in the dIGal could be caused by infalling gas from the cosmic web, but if this is true, should we not observe a gradient in metallicity in Fig. 9 instead of the homogeneous distribution that is actually observed? As we have seen, the gas in the dIGal is subject to the interaction with Mrk 1172 and to the inner kinematics of the galaxy. In a scenario of accretion is possible that this metal deficient content has mixed with the ISM.

Therefore our *conclusions about the nature of this object is that it is a dwarf irregular galaxy interacting with the massive ETG Mrk 1172.* It contains young stellar populations that have formed recently, and shows evidence of ongoing star formation. The star formation seems to be taking place mainly in clumpy knots along the structure of the galaxy. The gas phase of the galaxy is metal-poor, which could be related to infalling gas from the cosmic web, although we lack the information to support this hypothesis. To further investigate this hypothesis, observations of cold molecular gas would be needed, and, to the best of our knowledge, so far these observations are not available.

5 SUMMARY AND CONCLUSIONS

In this work we present a characterisation of chemical and physical properties of a dwarf galaxy (SDSS J020536.84−081424.7; dIGal)

located approximately 2.5 arcsec from the ETG Mrk 1172. To the best of our knowledge, the spectrum of this galaxy was not presented in the literature before, thus the analysis of this work is unprecedented. Below, we summarize the main conclusions of this work:

(i) Despite its low SNR in the continuum, the spectra of the dIGal presents strong emission lines, namely: H α, H β, [O III] $\lambda\lambda4959 + 5007$, [N II] $\lambda\lambda6548 + 6583$, and [S II] $\lambda\lambda6716 + 6731$. The stellar population synthesis reveals that Mrk 1172 is predominantly dominated by old stellar populations with $t \geq 10^{10}$ yr, while the dIGal contains young to intermediate-age stellar populations, with ages of $10^7 \sim 10^8$ yr and 10^9 yr. From analysis of the light-weighed stellar populations, we conclude that both galaxies have very different SFHs.

(ii) From the stellar content of the dIGal and Mrk 1172, we are able to estimate the stellar mass of both galaxies. We obtain $M_\star \sim 1.2 \times 10^{11} M_\odot$ for Mrk 1172, a value that lies close to a previous measurement found in the literature (Omand et al. 2014). The dIGal presents a stellar mass of $M_\star \sim 3 \times 10^9 M_\odot$, which is comparable to the mass of dwarf galaxies like the SMC ($M_\star = 6.5 \times 10^9 M_\odot$; Bekki & Stanimirović 2009) and to the BCDG Henize 2–10 ($M_\star = 3.7 \times 10^9 M_\odot$; Reines et al. 2011), for example. We have also estimated the lower limit of $3.8 \times 10^5 M_\odot$ for the ionized gas mass.

(iii) In order to investigate the gas excitation mechanism, we perform a spatially resolved study making use of emission-line diagnostic diagrams such as the BPT. Both diagrams indicate that the gas within the dIGal is being photoionized by young massive hot stars rather than by an AGN. Shock models are also investigated, but they are negligible.

(iv) The metallicity of the ionized gas phase of the dIGal is $\log(O/H) + 12 = 8.28 \pm 0.03$ for the O3N2 index, $\log(O/H) + 12 = 8.296 \pm 0.004$ for the N2 index and $\log(O/H) + 12 = 8.2 \pm 0.2$ when considering the calibration independent of ionization parameters from Dopita et al. (2016). These values represent an overall metallicity of approximately $1/3\ Z_\odot$ for the dIGal. This galaxy can be considered metal deficient, presenting typical values for dIs.

(v) Our measurements and observations strongly suggest that the dIGal is actively forming stars. We observe clumpy knots in H α emission along the structure of the dIGal, which we interpret as being sites of active star formation. We obtain an integrated value of SFR $= 0.70$ M$_\odot$ yr^{-1}; $\sum_{SFR} = 1.4 \times 10^{-2}$ M$_\odot$ yr^{-1} kpc^{-2}, and a $\log(\text{sSFR}) = -9.63$. The latter differs significantly from a previous measurement of $\log(\text{sSFR}) = -10.85$ found in the literature (DV19). We attribute this difference to the quality of photometric data for the dIGal (flagged as medium in DV19) and the distinct procedures adopted in both works.

(vi) Radial velocity maps indicate a trend in the motion of the gas, which seems to be in rotation. Using the velocity field considering H α and the stellar velocity field of Mrk 1172 we fit a kinematic model that considers a gas orbiting in a plane of a disc. From this fit, we observe that the position angle of the line of the nodes and the disc inclination are similar for both galaxies, thus indicating that the motion of the gas is being affected by the ETG. We thus conclude that both galaxies are interacting.

From the results summarized above, we conclude that the faint nebular emission-line region close in projection to Mrk 1172 is actually a gas-rich low-metallicity dwarf galaxy, most likely a dwarf irregular. The origin of this galaxy is still uncertain, and we are still unsure as to which specific processes triggered the recent star formation episodes in the dIGal. Bright knots are readily visible in the H α images of the dIGal, where the highest fraction of its stellar

content seems to be located. Detailed analysis of these knots and how they are ionizing the surrounding gas may shed more light on the nature and origins of the dIGal. With access to images with lower seeing, velocity sliced Hα maps of the dIGal (i.e. the analysis of Haro 11 in Menacho et al. 2019) may help to probe the internal structure of the galaxy. We are interested in the sizes of these knots, since they are seeing limited in MUSE data. With good spatial resolution in the NIR, for example, we can search for sub-structures in these knots and model surface brightness profiles for them. Modelling the light profile of both galaxies is essential to improve our understanding on their detailed structure, which can trace mergers in the past history of both systems. It also allows us to measure the Cluster Formation Efficiency, defined as the fraction of total stellar mass formed in clusters per unit time in a given age interval divided by the SFR of the region where the clusters are detected. This quantity relates to the SFR surface density to quantify the intrinsic connection between massive star cluster formation processes and the mean properties of the host galaxies and compare to other galaxies, including dwarf irregulars and BCDGs (Adamo, Östlin & Zackrisson 2011; Adamo et al. 2020). This posterior analysis may help us to understand better how this metal-deficient galaxy is interacting with Mrk 1172 by improving the accuracy in its distance estimate, and thus shed some light about the formation and evolution of such systems. All these efforts are, however, beyond the scope of this paper, and are left for a future publication.

DATA AVAILABILITY

The data used in this paper is available at ESO Science Archive Facility under the program-ID of 099.B-0411(A).

REFERENCES

Adamo A. et al., 2020, Space Sci. Rev., 216, 69
Adamo A., Östlin G., Zackrisson E., 2011, MNRAS, 417, 1904
Ahn C. P. et al., 2012, ApJS, 203, 21
Allen M. G., Groves B. A., Dopita M. A., Sutherland R. S., Kewley L. J., 2008, ApJS, 178, 20
Alloin D., Collin-Souffrin S., Joly M., Vigroux L., 1979, A&A, 78, 200
Aloisi A. et al., 2007, ApJ, 667, L151
Andrews B. H., Martini P., 2013, ApJ, 765, 140
Bacon R. et al., 2010, in McLean I. S., Ramsay S. K., Takami H., eds, SPIE Conf. Ser. Vol. 7735, Ground-based and Airborne Instrumentation for Astronomy III. SPIE, Bellingham, p. 773508
Baldwin J. A., Phillips M. M., Terlevich R., 1981, PASP, 93, 5
Bekki K., Stanimirović S., 2009, MNRAS, 395, 342
Bernard E. J. et al., 2010, ApJ, 712, 1259
Bertola F., Bettoni D., Danziger J., Sadler E., Sparke L., de Zeeuw T., 1991, ApJ, 373, 369
Cardelli J. A., Clayton G. C., Mathis J. S., 1989, ApJ, 345, 245
Ceverino D., Sánchez Almeida J., Muñoz Tuñón C., Dekel A., Elmegreen B. G., Elmegreen D. M., Primack J., 2016, MNRAS, 457, 2605
Cid Fernandes R. et al., 2013, A&A, 557, A86
Cid Fernandes R. et al., 2014, A&A, 561, A130
Cid Fernandes R., González Delgado R. M., 2010, MNRAS, 403, 780
Cid Fernandes R., Mateus A., Sodré L., Stasińska G., Gomes J. M., 2005, MNRAS, 358, 363
Croxall K. V., van Zee L., Lee H., Skillman E. D., Lee J. C., Côté S., Kennicutt Robert C. J., Miller B. W., 2009, ApJ, 705, 723
Dalcanton J. J., 2007, ApJ, 658, 941
Dekel A., Sari R., Ceverino D., 2009, ApJ, 703, 785
Delli Veneri M., Cavuoti S., Brescia M., Longo G., Riccio G., 2019, MNRAS, 486, 1377
Digby R. et al., 2019, MNRAS, 485, 5423
do Nascimento J. C. et al., 2019, MNRAS, 486, 5075
Dopita M. A., Kewley L. J., Sutherland R. S., Nicholls D. C., 2016, Ap&SS, 361, 61
ESO CPL Development Team, 2015, Astrophysics Source Code Library, record ascl:1504.003
Fattahi A., Navarro J. F., Frenk C. S., Oman K. A., Sawala T., Schaller M., 2018, MNRAS, 476, 3816
Gallart C. et al., 2015, ApJ, 811, L18
Gibson B. K., Matteucci F., 1997, ApJ, 475, 47
Gil de Paz A., Madore B. F., Pevunova O., 2003, ApJS, 147, 29
González Delgado R. M., Cid Fernandes R., 2010, MNRAS, 403, 797
González-Samaniego A., Colín P., Avila-Reese V., Rodríguez-Puebla A., Valenzuela O., 2014, ApJ, 785, 58
Hinshaw G. et al., 2013, ApJS, 208, 19
Jordi K., Grebel E. K., Ammon K., 2006, A&A, 460, 339
Kauffmann G. et al., 2003, MNRAS, 346, 1055
Kazantzidis S., Łokas E. L., Callegari S., Mayer L., Moustakas L. A., 2011, ApJ, 726, 98
Kennicutt Robert C. J., 1998, ARA&A, 36, 189
Kewley L. J., Dopita M. A., Sutherland R. S., Heisler C. A., Trevena J., 2001, ApJ, 556, 121
Kewley L. J., Groves B., Kauffmann G., Heckman T., 2006, MNRAS, 372, 961
Kewley L. J., Zahid H. J., Geller M. J., Dopita M. A., Hwang H. S., Fabricant D., 2015, ApJ, 812, L20
Kirby E. N., Cohen J. G., Guhathakurta P., Cheng L., Bullock J. S., Gallazzi A., 2013, ApJ, 779, 102
Kormendy J., Bender R., 2012, ApJS, 198, 2
Kunth D., Östlin G., 2000, A&AR, 10, 1
Lequeux J., Peimbert M., Rayo J. F., Serrano A., Torres-Peimbert S., 1979, A&A, 500, 145
Mallmann N. D. et al., 2018, MNRAS, 478, 5491
Marino R. A. et al., 2013, A&A, 559, A114
Mashchenko S., Wadsley J., Couchman H. M. P., 2008, Science, 319, 174
Mateo M. L., 1998, ARA&A, 36, 435
Mayer L., Governato F., Colpi M., Moore B., Quinn T., Wadsley J., Stadel J., Lake G., 2001, ApJ, 547, L123
Menacho V. et al., 2019, MNRAS, 487, 3183

Monreal-Ibero A., Relaño M., Kehrig C., Pérez-Montero E., Vílchez J. M., Kelz A., Roth M. M., Streicher O., 2011, MNRAS, 413, 2242

Nagao T., Maiolino R., Marconi A., 2006, A&A, 459, 85

Navarro J. F., Eke V. R., Frenk C. S., 1996, MNRAS, 283, L72

O'Donnell J. E., 1994, ApJ, 422, 158

Omand C. M. B., Balogh M. L., Poggianti B. M., 2014, MNRAS, 440, 843

Osterbrock D. E., Ferland G. J., 2006, Astrophysics of Gas Nebulae and Active Galactic Nuclei. University Science Books. California, USA

Pérez-Montero E., Contini T., 2009, MNRAS, 398, 949

Pettini M., Pagel B. E. J., 2004, MNRAS, 348, L59

Pilyugin L. S., Ferrini F., 2000, New Astron. Rev., 44, 335

Reines A. E., Sivakoff G. R., Johnson K. E., Brogan C. L., 2011, Nature, 470, 66

Revaz Y., Jablonka P., 2018, A&A, 616, A96

Riffel R. et al., 2021, MNRAS, 501, 4064

Riffel R., Pastoriza M. G., Rodríguez-Ardila A., Bonatto C., 2009, MNRAS, 400, 273

Rubin V. C., Ford W. K. J., Whitmore B. C., 1984, ApJ, 281, L21

Ruschel-Dutra D., de Oliveira B. D., 2020, danielrd6/ifscube: Modeling (Version v1.1). Available at: http://doi.org/10.5281/zenodo.4065550

Ryden B., Pogge R., 2021, Interstellar and Intergalactic Medium. Cambridge University Press, Cambridge

Sánchez Almeida J. et al., 2015, ApJ, 810, L15

Schlegel D. J., Finkbeiner D. P., Davis M., 1998, ApJ, 500, 525

Skillman E. D., Bender R., 1995, Rev. Mex. Astron. Astrofis. Ser. Conf., 3, 25

Skillman E. D., Kennicutt R. C., Hodge P. W., 1989, ApJ, 347, 875

Soto K. T., Lilly S. J., Bacon R., Richard J., Conseil S., 2016, MNRAS, 458, 3210

Steffen M., Prakapavičius D., Caffau E., Ludwig H. G., Bonifacio P., Cayrel R., Kučinskas A., Livingston W. C., 2015, A&A, 583, A57

Steyrleithner P., Hensler G., Boselli A., 2020, MNRAS, 494, 1114

Storchi-Bergmann T., Calzetti D., Kinney A. L., 1994, ApJ, 429, 572

Tremonti C. A. et al., 2004, ApJ, 613, 898

van der Kruit P. C., Allen R. J., 1978, ARA&A, 16, 103

van Zee L., 2001, AJ, 121, 2003

van Zee L., Haynes M. P., 2006, ApJ, 636, 214

Vazdekis A., Sánchez-Blázquez P., Falcón-Barroso J., Cenarro A. J., Beasley M. A., Cardiel N., Gorgas J., Peletier R. F., 2010, MNRAS, 404, 1639

Vazdekis A., Koleva M., Ricciardelli E., Röck B., Falcón-Barroso J., 2016, MNRAS, 463, 3409

Weilbacher P. M. et al., 2020, A&A, 641, A28

Wylezalek D. et al., 2017, MNRAS, 467, 2612

This paper has been typeset from a TeX/LaTeX file prepared by the author.